Journal of Power Sources 202 (2012) 120–125

Contents lists available at SciVerse ScienceDirect

Journal of Power Sources

journal homepage: www.elsevier.com/locate/jpowsour

Free standing oxide alloy electrolytes for low temperature thin film solid oxide fuel cells

Kian Kerman *,[1], Bo-Kuai Lai [1], Shriram Ramanathan

Harvard School of Engineering and Applied Sciences, Cambridge, MA 02138, USA

ARTICLE INFO

Article history:
Received 21 October 2011
Received in revised form
19 November 2011
Accepted 21 November 2011
Available online 28 November 2011

Keywords:
Thin film solid oxide fuel cell
alloy electrolyte
Free standing
YSZ
CGO
Co-sputtering

ABSTRACT

Thermomechanical challenges place restrictions on the choice of fast ion conductors that may be implemented as free standing electrolyte membranes for low temperature solid oxide fuel cells. In order to expand the possible choices, mechanical and chemical stability constraints must be taken into consideration. Here, we present a method to utilize the mechanical stability of a ZrO_2 based electrolyte for this application. Facile low temperature synthesis of solid solution $(Y_2O_3)_{0.08}(ZrO_2)_{0.92}$–$(Gd_2O_3)_{0.1}(CeO_2)_{0.9}$ free standing electrolytes by co-sputtering is demonstrated. Fuel cells integrating these nanoscale electrolytes show power output of over 1000 mW cm^{-2} at 510 °C and are thermomechanically robust. The results demonstrate a general route for low temperature synthesis of nanoscale functional oxide alloys for thin film solid oxide fuel cells.

1. Introduction

Solid oxide fuel cells (SOFCs) are electrochemical devices capable of directly converting chemical energy into electrical energy. They include three main components, namely the anode, cathode, and electrolyte. These components refer to the electrode where oxidation takes place, electrode where reduction takes place, and the ionically conductive, electrically insulating separator between electrodes, respectively. When the mobile ionic species in SOFCs is oxygen (O^{2-}), ionic conductors capable of sufficiently fast transport generally require elevated temperature (800–1000 °C) [1]. The operation temperature must be reduced significantly in order to improve material stability, reduce start-up time, and extend the applications of SOFCs to mobile power units. High performance of SOFCs at reduced temperatures can be achieved by minimizing total loss across the entire cell. Kinetic losses at the anode and cathode make up two of the three main losses. The third comes from loss associated with O^{2-} ion transport in the electrolyte, which is ohmic in nature. It can be counteracted by designing electrolyte materials with increased ionic conductivity at low temperature or reducing electrolyte thickness as low as physically possible without significant electronic leakage. For these reasons, free standing thin film solid oxide fuel cells (TF-SOFCs) based on nanocrystalline $(Y_2O_3)_y(ZrO_2)_{(1-y)}$electrolytes with Pt electrodes have been recently explored [2–7].

High performance has been achieved with optimized electrodes and corrugated electrolyte structures [7,8]. Huang et al. showed that enhanced kinetics of the oxygen reduction reaction (ORR) and improved TF-SOFC performance at low temperature can be realized using a Gd doped CeO_2 (CGO) interlayer on the cathode [2]. Gauckler and co-workers have characterized the various components of TF-SOFCs [9–11]. They have elucidated the challenges in producing a dense, chemically inert, thin film electrolyte necessary for high performance TF-SOFCs operating at low temperatures. $(Gd_2O_3)_{(z)}(CeO_2)_{(1-z)}$ is well known for its superior ionic conductivity at low temperature [12,13]. In addition, CeO_2 has been shown to be an active electrocatalyst for hydrocarbon oxidation [14]. Kossoy et al. have explored the stability of self-supported CGO [15]. It was found that the association/dissociation reaction:

$$Gd'_{Ce} + V_O^{\bullet\bullet} \Leftrightarrow [Gd'_{Ce}V_O^{\bullet\bullet}]^{\bullet}$$

plays a strong role in volumetric deformations at low temperatures ($T < 200$ °C). Above 250 °C, the authors state that the film does not exhibit anomalous elastic properties. In addition to temperature dependent stability, creating a working, high performance TF-SOFC with a free-standing electrolyte requires mechanical stability across oxygen partial pressure gradient. Wang et al. have elucidated this relationship for CGO and Y doped ZrO_2 (YSZ) [16]. It was shown that YSZ exhibits an elastic modulus independent

* Corresponding author. Tel.: +1 617 497 2746.
E-mail address: kkerman@fas.harvard.edu (K. Kerman).
[1] These authors contributed equally.

0378-7753/$ – see front matter © 2011 Elsevier B.V. All rights reserved.
doi:10.1016/j.jpowsour.2011.11.062

of $P(O)_2$, while CGO does not. This has been attributed to the formation of Ce^{3+} at low $P(O)_2$, which leads to an increase in the average bond length, altering the elastic modulus [17]. This complex interplay between chemical and mechanical properties makes utilizing free standing CGO membranes for low temperature TF-SOFCs rather challenging. These challenges have limited the choice of materials for research and development in such applications. In this report, we demonstrate successful low temperature synthesis by physical vapor deposition of thin film mixtures of $[(Y_2O_3)_{0.08}(ZrO_2)_{0.92}]_x[(Gd_2O_3)_{0.1}(CeO_2)_{0.9}]_{(1-x)}$ ($YSZ_xCGO_{(1-x)}$), where x is the volume fraction of each component. These films are chemically and mechanically stable during SOFC operation. Traditional processing of similar composites requires temperatures of over 1300 °C to achieve solid solution mixtures [18,19]. Moreover, formation of defects at YSZ–CGO interfaces during high temperature sintering has been reported [20]. The method of co-sputtering addresses these significant issues and has the potential to create nanostructured materials with a controllable ratio of constituents, nanoscale control of physical structures, and reduced processing temperatures. Here, we demonstrate this approach in the context of free standing TF-SOFCs. The aim of this study is to show that mechanical constraints limiting the choice of materials can be overcome in an elegant way by exercising techniques available in thin film deposition. Films synthesized in this study demonstrate the feasibility of processing thin film-based membranes and show encouraging high TF-SOFC performance at low temperatures using an ultra-thin, oxide alloy electrolyte material.

2. Experimental

2.1. Thin film growth and characterization

$YSZ_xCGO_{(1-x)}$ films were grown by radio-frequency sputtering from stoichiometric targets of $(Y_2O_3)_{0.08}(ZrO_2)_{0.92}$ and $(Gd_2O_3)_{0.1}(CeO_2)_{0.9}$ in an Ar atmosphere, at a pressure of 5 mTorr, with a substrate temperature of 550 °C or 25 °C. Thickness and growth rate of each constituent material was calibrated by X-ray reflectivity. By altering deposition time while keeping target power constant, the growth rate was determined. Similarly, by altering target power while keeping deposition time constant, the target power dependence was obtained. The electrolyte films explored in this study were ~100 nm in thickness. Glancing incidence, $\Omega = 1°$, X-ray diffraction (XRD) of films grown on Si_3N_4 coated Si was used to study the crystal structure and phase. A JEOL 2100 transmission electron microscope (TEM) was used to investigate the local polycrystalline grain structure of the films. TEM samples were prepared by manual lapping followed by ion milling to electron transparency using a Fischione 1010 ion mill. In-plane conductivity of films grown at 550 °C was measured in air using a direct current (DC) method with sputtered Pt electrodes as a function of temperature every 2° up to 550 °C at a heating rate of 2 °C min^{-1}.

2.2. TF-SOFC fabrication and testing

Free standing membranes were created by patterning Si_3N_4 coated Si wafers followed by subsequent dry and wet etching steps to reveal Si_3N_4 windows of desired dimensions. The patterned square windows used in this study were 160 μm × 160 μm. Further details on this fabrication method can be found elsewhere [3,7]. Electrolyte films were then grown at 550 °C on such patterned substrates. Upon removal of the underlying Si_3N_4 window by dry reactive ion etching, the film becomes a free standing square membrane, anchored at the edges. Buckling deformation after substrate removal was observed by optical microscopy at room temperature. TF-SOFCs were made by growing nanoporous Pt on both sides of the sample by DC sputtering at a pressure of 75 mTorr without substrate heating. Fuel cell testing was carried out using an Ar carrier gas with 5% H_2 as fuel. The fuel was humidified with 3% H_2O and heated before reaching the anode. The oxidant employed at the cathode during testing was standing laboratory air.

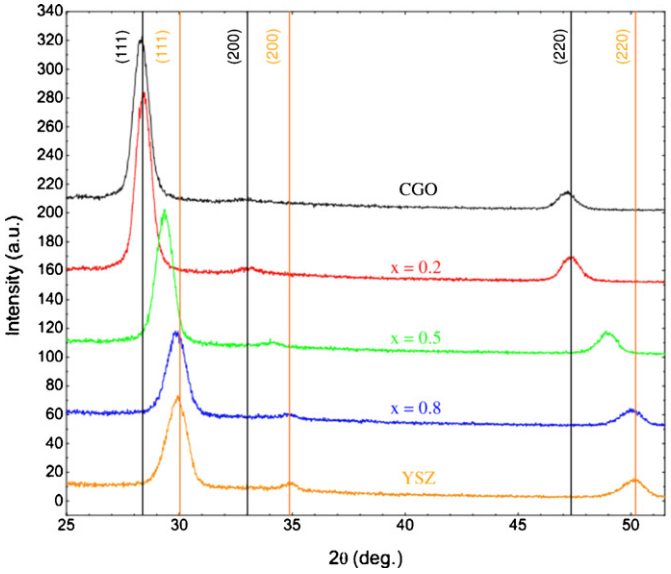

Fig. 1. Glancing incidence XRD patterns of nanostructured alloy thin films grown by co-sputtering with YSZ and CGO peaks indexed to ICDD 030-1468 and 01-075-0161, respectively.

3. Results and discussion

3.1. Material characterization

Fig. 1 shows the XRD patterns of CGO, $YSZ_{0.2}CGO_{0.8}$, $YSZ_{0.5}CGO_{0.5}$, $YSZ_{0.8}CGO_{0.2}$, and YSZ films grown at 550 °C. The XRD pattern shows the existence of a cubic fluorite crystal structure with varying lattice parameter between that of YSZ and CGO. Similar results were obtained for composites grown without substrate heating, indicating a substantial decrease in processing temperature for such materials. For $x = 0.5$, the (1 1 1) d-spacing can be

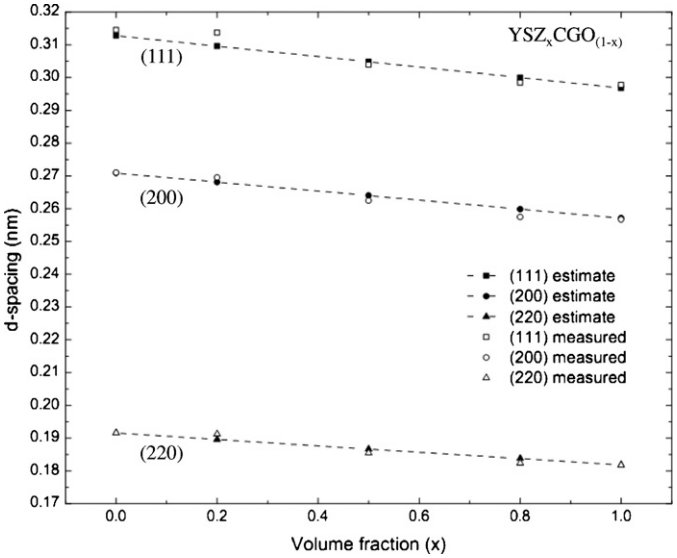

Fig. 2. Plot of ideal Vegardian behavior and experimental planar spacing shown with closed and open symbols, respectively.

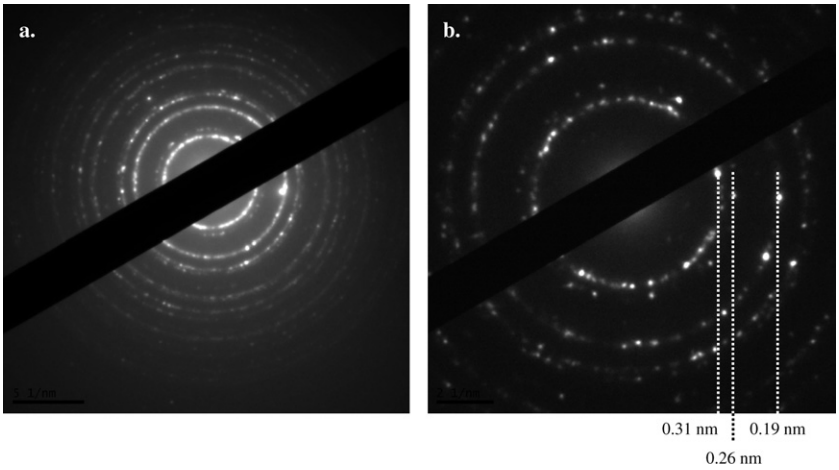

Fig. 3. (a) SAED pattern of $x = 0.5$ YSZ–CGO electrolyte film with (b) measured ring spacing for (1 1 1), (2 0 0), and (2 2 0) planes.

estimated as 0.305 nm from Vegard's law [21]. This agrees well with the experimentally measured value of 0.30 nm. Similar trends were found for (2 0 0) and (2 2 0) spacing; the measured and estimated values are plotted in Fig. 2. Fig. 3 shows a selected area diffraction (SAED) pattern of the $x = 0.5$ film. Ring patterns confirm the polycrystalline nature observed by XRD. Since the area of investigation is profoundly smaller than that of XRD, average lattice spacing from several spatially separated SAED patterns were necessary to determine an accurate estimate of the various d-spacings in the film. The innermost rings correspond to the smallest reciprocal space length and hence the largest real d-spacing, which in this case should be (1 1 1). Based on the results of XRD, a single ring with spacing of approximately 0.305 nm is expected. The measured spacing of 0.31 nm corresponds reasonably well within a single standard deviation of the averaged measurements. The (2 0 0) spacing was measured to be 0.26 nm which corresponds to the estimated value of 0.264 nm from Vegard's law. Similarly, (2 2 0) spacing was found to be 0.19 nm corresponding well to 0.187 nm from Vegard's law. Fig. 4 shows bright field, dark field, and high resolution TEM plan view images of the $x = 0.5$ film. It can be seen that the average grain size is on the order of 20 nm. The lattice spacing estimated from the high resolution image shown in Fig. 4(d) was 0.26 nm, which

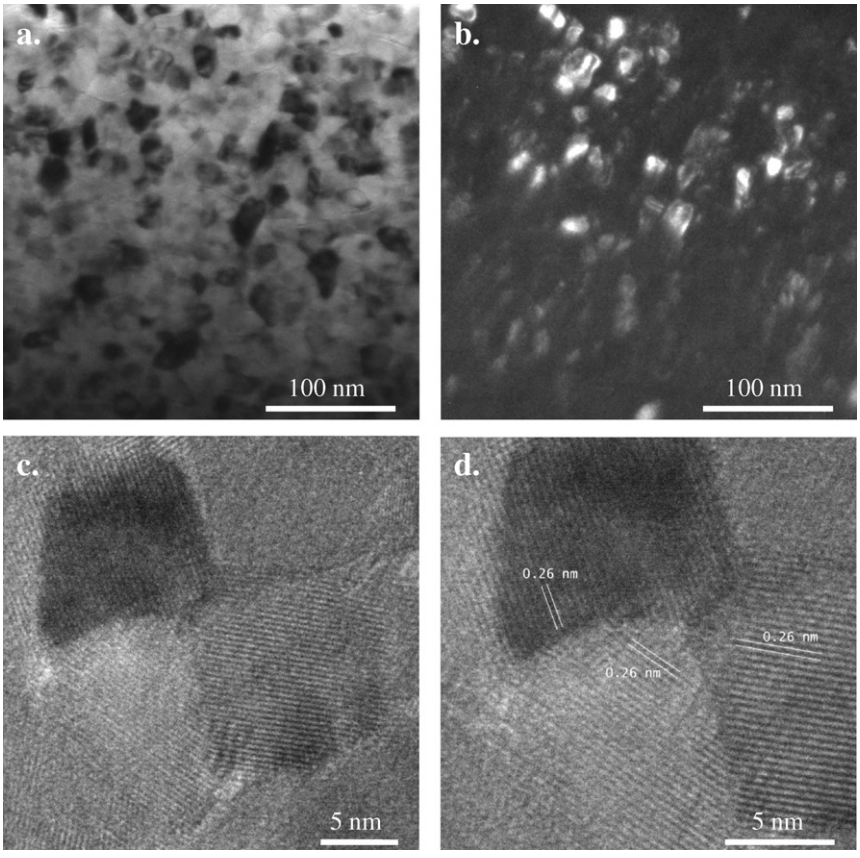

Fig. 4. (a) Bright field; (b) dark field plan view TEM image of the nanocrystalline structure of $x = 0.5$ film; (c) high resolution TEM image of a triple junction and (d) high resolution TEM image with measured lattice spacing.

Table 1
The activation energy for conduction of $YSZ_xCGO_{(1-x)}$ films as function of volume fraction (x).

x	E_a (eV)
0	0.84
0.2	1.30
0.5	1.14
0.8	1.13
1	1.05

agrees well with the discussion above for (2 0 0) spacing. Based on these results, solid solution of YSZ and CGO seems likely in these films.

3.2. Electrical conductivity

Fig. 5 shows the conductivity of the composite film electrolytes grown at 550 °C on Si_3N_4 coated Si measured in air. Under the oxygen partial pressure conditions of air, both YSZ and CGO are known to be in the ionic conduction regime [22,23]. These results represent the total conductivity of the films. The results are consistent with the activation energy for YSZ and CGO reported in the literature. Following an activated Arrhenius type mechanism for conduction;

$$\sigma_i = \left(\frac{A}{T}\right) e^{(-E_a/kT)}$$

where σ_i is ionic conductivity, A is a material specific constant, T is absolute temperature, k is the Boltzmann's constant, and E_a is activation energy; E_a was calculated in the 250–550 °C range for all compositions. The estimated value of 1.05 eV for YSZ ($x = 1$) is in agreement with values reported across the literature [12,23]. In the case of CGO ($x = 0$), E_a was estimated to be 0.84 eV. This finding indicates grain boundary dominated transport [24]. This observation is not unreasonable considering the nanostructured polycrystalline nature of the films. The activation energy for conduction in the solid solution mixtures of YSZ–CGO are shown in Table 1. They range from 1.1 to 1.3 eV and decrease monotonically as the fraction of CGO is decreased. This is similar to what has been previously reported for such mixtures produced by solid-state reaction [25]. Solid solution of these phases has been reported to show lower total conductivity than that of each constituent [25,26]; however a tunable ionic conductivity is observed across the range of compositions tested in this study.

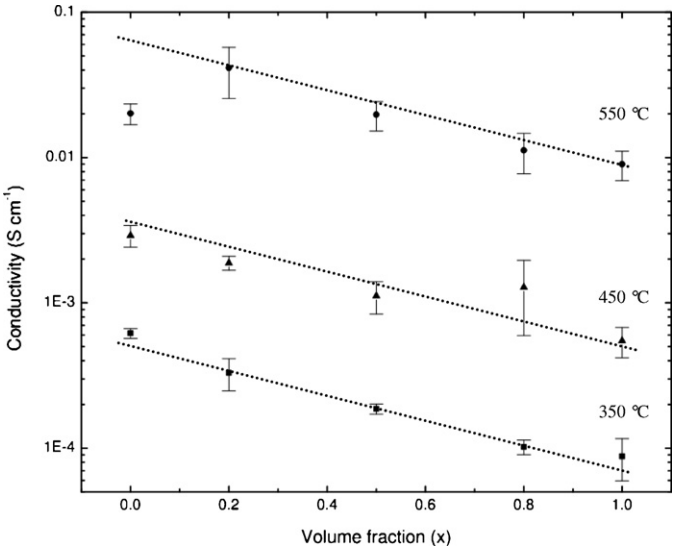

Fig. 5. Electrical conductivity of nanostructured films measured in air as a function of composition at 350 °C, 450 °C, and 550 °C. Error bars correspond to $\pm 3\sigma$. Temperature fluctuations were less than ±2°.

3.3. Free standing membrane stability

The mechanical stability of free standing membranes was evaluated with 100 nm electrolytes grown on micro machined Si_3N_4 coated Si substrates as described in Section 2. Films grown at 550 °C were released from the underlying patterned substrate, creating a free standing membrane that is bounded by the original substrate not etched away. In order to be used for high performance free-standing TF-SOFCs, the membranes must maintain mechanical integrity through many heating and cooling cycles. Optical micrographs in Fig. 6 show the mechanical response of such membranes immediately after being released at 25 °C. The material response is due to residual strain in the films, described in detail below. It is manifested by non-linear buckling of the free standing structures. The two main modes of buckling observed in all samples tested are shown as a function of composition. Similar to previous works, four-fold rotational symmetry in YSZ membranes is observed in both modes [7,27], however, CGO membranes fail in all cases. Looking across the composition, there is a distinct shift in macroscopic buckling behavior when crossing the $x = 0.5$ composition electrolyte. Buckling is largely dependent on pre-strain present in the free standing material, expressed in simplified form below [28,29]:

$$\langle \varepsilon_0 \rangle = \varepsilon_0 \left(\frac{a^2}{h^2}\right)$$

where ε_0 represents physical pre-strain, a is the width of the membrane, and h is the membrane thickness. In this study, the membrane thickness and width was kept constant. Additionally, the growth rate of each constituent material was maintained at approximately 1 nm min^{-1} and the cooling rate equivalent for all films. Therefore, the only modulation of pre-strain occurs as a material property of $YSZ_xCGO_{(1-x)}$ films as a function of x. Earlier work on similar membranes highlighted the importance of compressive strain for stability [30]. Out of plane displacement in the buckling patterns shown in Fig. 6 is a clear indication of compressive strain relief. The thermal expansion coefficients of YSZ and CGO are comparable at 550 °C [31,32], however, there is a slight difference in the temperature dependence of thermal expansion. Therefore, the origin of different pre-strains in these films lies in thermomechanically induced film stress and the stability and co-existence of Ce^{3+} and Ce^{4+}, which largely alters oxygen vacancy concentration. The elastic modulus of CGO is strongly altered by oxygen vacancy concentration, while that of YSZ is not [16,17]. By altering the fraction of each component in the single fluorite crystal synthesized, the internal pre-strain is modulated and hence, the mechanical buckling behavior of the membranes is directly affected. The membranes were thermally cycled to determine if they would be suitable for TF-SOFC application. In this study, only free standing membranes with compositions having $x \geq 0.5$, survive two heating cycles from 25 °C to 550 °C. These results suggest that the mechanical limitations for free standing thin film electrolytes can be overcome by tuning strain in films by altering composition. Other methods to engineer strain make it possible to extend the composition range by tuning film processing parameters [33,34].

3.4. Low temperature TF-SOFC performance

TF-SOFCs were fabricated using a 100 nm thick $x = 0.5$ electrolyte. This electrolyte represents the largest departure from YSZ (i.e. $x = 1$) that is mechanically stable. Using a stable thin film membrane such as those presented here, extending the active side

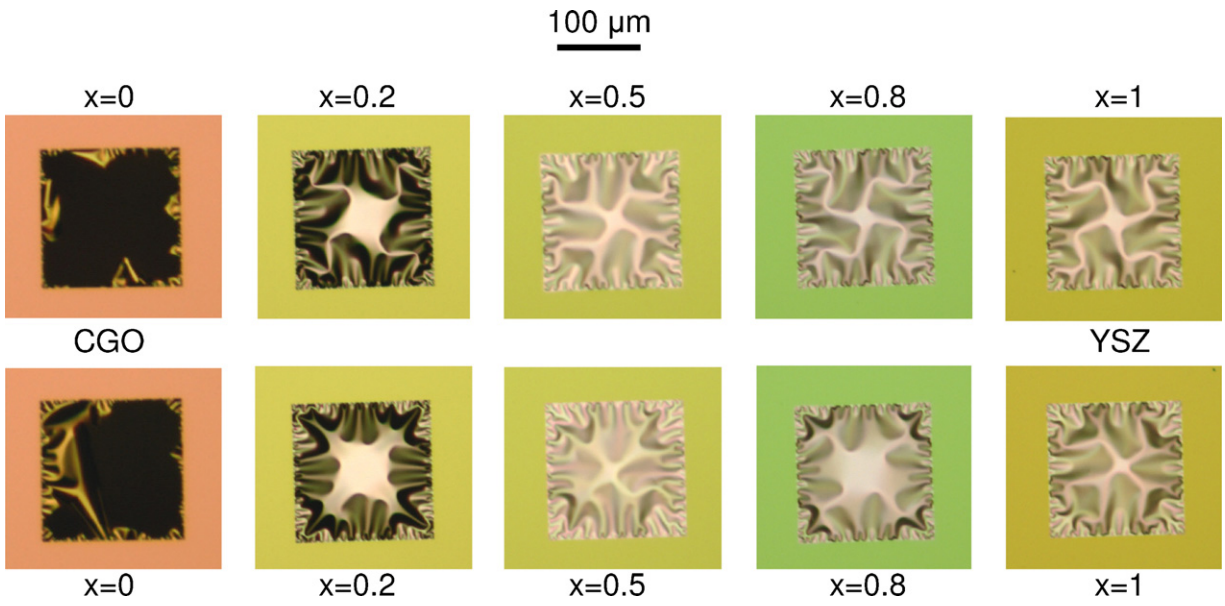

Fig. 6. Optical micrographs of the dominant buckling responses formed by free standing thin film electrolytes. Free standing films of pure CGO failed catastrophically and resulted in structures that could not span the unsupported area.

length of TF-SOFCs to centimeters is possible [35]. Performance and schematic of the mechanically stable free standing TF-SOFCs is shown in Fig. 7. A maximum power density of 1025 mW cm^{-2} was obtained with an open circuit voltage (OCV) of 0.413 V at 510 °C. This is in the range of power densities reported for high performance thin film solid oxide fuel cells with Pt electrodes [2,7,8]. Explanation for the deviation of the measured OCV to the Nernst potential of 1.06 V at this temperature is likely due to a percolating electronic path through the membrane, as it is known that the mixed valence of Ce leads to a non-negligible electronic

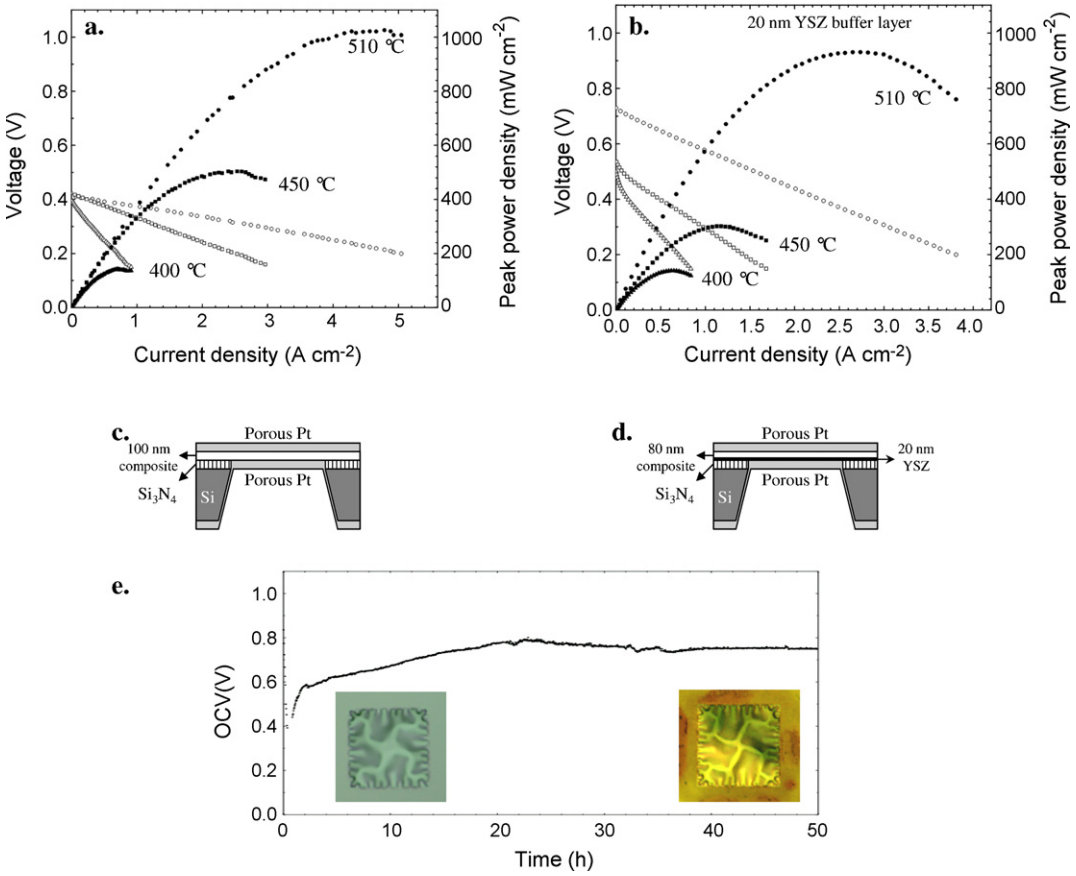

Fig. 7. (a) and (c) Performance and schematic of mechanically stabilized oxide alloy electrolyte based TF-SOFCs, (b) and (d) performance and schematic of a mechanically stabilized TF-SOFC with a YSZ buffer layer to prevent electronic leakage, and (e) OCV of structure (d) under measurement conditions at 450 °C for 50 h. The inset shows optical images of the TF-SOFC before and after testing.

contribution to its total conductivity in reducing atmospheres and the addition of YSZ leads to increased electronic conductivity [12,14]. The linear region of the *I–V* curve corresponds to the ohmic loss associated with O^{2-} transport across the electrolyte. Similar high performance TF-SOFCs have been fabricated with YSZ electrolytes [7]; however the area specific resistance (ASR) of such TF-SOFCs was on the order of $0.083\,\Omega\,cm^2$. TF-SOFCs presented here have an ASR half as large, $0.041\,\Omega\,cm^2$. The inability to achieve ideal OCV creates a large drop in voltage efficiency. In an attempt to circumvent electronic leakage, a 20 nm buffer layer of YSZ was integrated into the structure on the anode side. The performance and schematic of this configuration is also shown in Fig. 7. Power output of $930\,mW\,cm^{-2}$ was measured with an increased OCV of 0.73 V, indicating that leakage across the membrane due to the mixed valence of Ce does play a role in the observed OCV deviation. Since a 20 nm blocking layer does not completely address this issue, other factors may be of concern. For example, 20 nm YSZ may not provide a large enough barrier to electronic leakage. The thinnest free standing electrolyte with near ideal OCV reported is 27 nm [7]. Additionally, though we do not observe any pin-holes or voids, deviations of OCV from the theoretical value in TF-SOFCs is often attributed to partial fuel crossover or leakage due to microstructural defects [4,5,36]. There is an interesting temperature dependence of the OCV. Should microstructural defects be initially present and subsequently healed during heating, it may explain the jump in OCV observed. The mechanical stability of the free standing composite membrane was further explored by leaving the TF-SOFC at 450 °C for 50 h under measurement conditions. Similar to previous reports, performance degradation occurred due to microstructural change in the electrodes [7,8]; however Fig. 7(e) shows that after such changes, a stable OCV was maintained. This is an encouraging indication of the structural and chemical stability of the free standing nanostructured electrolytes fabricated in this study.

4. Conclusions

We have fabricated free standing membranes based on oxide alloys by co-sputtering for low temperature solid oxide fuel cells. Free standing TF-SOFCs were demonstrated with an oxide alloy electrolyte and exhibited performance of over $1000\,W\,cm^{-1}$ at 510 °C using 5% H_2 as fuel and air as the oxidant.

Acknowledgement

The authors acknowledge NSF-CCF grant no. 0926148 for financial support.

References

[1] S.C. Singhal, K. Kendall, High Temperature Solid Oxide Fuel Cells, Elsevier, Oxford, UK, 2003.
[2] H. Huang, M. Nakamura, P.C. Su, R. Fasching, Y. Saito, F.B. Prinz, J. Electrochem. Soc. 154 (2007) B20–B24.
[3] A.C. Johnson, B.-K. Lai, H. Xiong, S. Ramanathan, J. Power Sources 186 (2009) 252–260.
[4] U.P. Muecke, D. Beckel, A. Bernard, A. Bieberle-Hütter, S. Graf, A. Infortuna, P. Müller, J.M. Rupp, J. Schneider, L.J. Gauckler, Adv. Funct. Mater. 18 (2008) 3158–3168.
[5] S. Rey-Mermet, P. Muralt, Solid State Ionics 179 (2008) 1497–1500.
[6] X. Chen, J. Wu, L. Smith, A. Ignatiev, Appl. Phys. Lett. 84 (2004) 2700.
[7] K. Kerman, B.-K. Lai, S. Ramanathan, J. Power Sources 196 (2011) 2608–2614.
[8] C.C. Chao, C.M. Hsu, Y. Cui, F.B. Prinz, ACS Nano 5 (2011) 5692–5696.
[9] A. Evans, A. Bieberle-Hutter, J.L.M. Rupp, L.J. Gauckler, J. Power Sources 194 (2009) 119–219.
[10] A. Bieberle-Hutter, P. Reinhard, J.L.M. Rupp, L.J. Gauckler, J. Power Sources 196 (2011) 6070.
[11] T. Ryll, J.L.M. Rupp, A. Bieberle-Hutter, H. Galinski, L.J. Gauckler, Scr. Mater. 65 (2011) 84–89.
[12] J.B. Goodenough, Annu. Rev. Mater. Res. 33 (2003) 91–128.
[13] S. Wang, T. Kobayahsi, M. Dokiya, T. Hashimoto, J. Electrochem. Soc. 147 (2000) 3606–3609.
[14] G. Kim, J.M. Vohs, R.J. Gorte, J. Mater. Chem. 18 (2008) 2386–2390.
[15] A. Kossoy, A.I. Frenkel, Y. Feldman, E. Wachtel, A. Milner, I. Lubomirsky, Solid State Ionics 33 (2010) 1473–1477.
[16] Y. Wang, K. Duncan, E.D. Wachsman, F. Ebrahimi, Solid State Ionics 178 (2007) 53–58.
[17] K. Duncan, Y. Wang, S. Bishop, F. Ebrahimi, E. Wachsman, J. Am. Ceram. Soc. 89 (2006) 3162–3166.
[18] M. Price, J. Dong, X. Gu, S.A. Speakman, E.A. Payzant, T.M. Nenoff, J. Am. Ceram. Soc. 18 (2005) 1812–1818.
[19] G.A. Tompsett, N.M. Sammes, O. Yamamoto, J. Am. Ceram. Soc. 80 (1997) 3181–3186.
[20] A. Tsoga, A. Gupta, A. Naoumidis, P. Nikolopoulos, Acta Mater. 48 (2000) 4709–4714.
[21] L. Vegard, Z. Phys. 5 (1921) 17–26.
[22] A. Podpirka, S. Ramanathan, J. Am. Ceram. Soc. 92 (2009) 2400–2403.
[23] H.D. Wiemhofer, H.G. Bremes, U. Nigge, W. Zipprich, Solid State Ionics 150 (2002) 63–77.
[24] H. Huang, T.M. Gur, Y. Saito, F.B. Prinz, Appl. Phys. Lett. 89 (2006) 143107.
[25] X.D. Zhou, B. Scarfino, H.U. Anderson, Solid State Ionics 175 (2004) 19.
[26] S. Hui, J. Roller, S. Yick, X. Zhang, C. Deces-Petit, Y. Xie, R. Maric, D. Ghosh, J. Power Sources 172 (2007) 493–502.
[27] B.-K. Lai, K. Kerman, S. Ramanathan, J. Power Sources 195 (2010) 5185–5196.
[28] V. Ziebart, O. Paul, H. Baltes, J. Microelectromech. Syst. 8 (1999) 423–432.
[29] S. Conti, A. DeSimone, S. Muller, Comput. Methods Appl. Mech. Eng. 184 (2005) 2534–2549.
[30] C.D. Baertsch, K.F. Jensen, J.L. Hertz, H.L. Tuller, S.T. Vengallatore, S.M. Spearing, M.A. Schmidt, J. Mater. Res. 19 (2004) 2604–2615.
[31] H. Hayashi, T. Saitou, N. Maruyama, H. Inaba, K. Kawamura, M. Mori, Solid State Ionics 176 (2005) 613–619.
[32] H. Hayashi, M. Kanoh, C.J. Quan, H. Inaba, S. Wang, M. Dokiya, H. Tagawa, Solid State Ionics 132 (2000) 227–233.
[33] B.-K. Lai, A.C. Johnson, H. Xiong, S. Ramanathan, J. Power Sources 186 (2009) 115–122.
[34] N. Yamamoto, D.J. Quinn, N. Wicks, J.L. Hertz, J. Cui, H.L. Tuller, B.L. Wardle, J. Micromech. Microeng. 20 (2010) 035027.
[35] M. Tsuchiya, B.-K. Lai, S. Ramanathan, Nat. Nanotechnol. 6 (2011) 282–286.
[36] J.H. Joo, G.M. Choi, J. Power Sources 182 (2008) 589–593.